Geochemistry Geophysics Geosystems G3
AN ELECTRONIC JOURNAL OF THE EARTH SCIENCES
Published by AGU and the Geochemical Society

Article
Volume 9, Number 8
19 August 2008
Q08009, doi:10.1029/2008GC002031
ISSN: 1525-2027

Synthetic aperture radar interferometry observations of the *M* = 6.0 Orta earthquake of 6 June 2000 (NW Turkey): Reactivation of a listric fault

Ziyadin Cakir
Faculty of Mines, Department of Geology, Istanbul Technical University, Maslak 34469, Istanbul, Turkey (ziyadin.cakir@itu.edu.tr)

Earth and Marine Sciences Institute, MRC, TUBITAK, Gebze, Izmit, Turkey

Ahmet Murat Akoglu
Eurasian Institute of Earth Sciences, Istanbul Technical University, Maslak 34469, Istanbul, Turkey (akoglua@itu.edu.tr)

[1] We study the coseismic surface displacement field due to the Orta earthquake of 6 June 2000, a moderate-sized (M_w 6.0) oblique-slip event that took place on a previously unknown fault located about 70 km north of the capital, Ankara (Turkey), and about 35 km south of the North Anatolian Fault. We use European Space Agency ERS synthetic aperture radar (SAR) data to generate high-resolution maps of the surface displacements by a two-pass differential SAR interferometry method. The surface displacement field reaching up to 15 cm line of sight subsidence is captured in several coseismic interferograms from descending orbits and is inverted to determine the source parameters of the earthquake using elastic dislocations on rectangular fault surfaces with a nonlinear minimization procedure based on simulating annealing algorithm. Modeling of the coseismic interferograms indicates that the earthquake was associated with a shallow (<6 km) left-lateral oblique normal displacement that occurred on a north-south striking, eastward dipping, listric fault trending at a high angle to the plate boundary, right-lateral strike-slip North Anatolian fault. Careful analyses of multiple interferograms together with the field observations allow us to infer the rupture geometry in fine detail. Modeling shows that coseismic slip occurs nearly only on the lower portion of the listric fault at a centroid depth of about 5 km but partially reaches to the surface along the surface trace of the Dodurga fault, in agreement with the field observations. We show that in the absence of field observations, additional measurements, or multiple interferograms that capture the surface deformation from different look angles, SAR interferometry alone may not be sufficient to constrain earthquake rupture geometry if there is no clear surface faulting. The results suggest that the Dodurga fault developed most probably as a result of a restraining bend along the North Anatolian fault and its left-lateral kinematics is consistent with the stress regime that favors the right-lateral North Anatolian fault.

Components: 9221 words, 10 figures, 2 tables.

Keywords: InSAR; Orta Cankiri earthquake; listric fault; active tectonics; North Anatolian Fault; fault parameters.

Index Terms: 1242 Geodesy and Gravity: Seismic cycle related deformations (6924, 7209, 7223, 7230); 8002 Structural Geology: Continental neotectonics (8107); 0480 Biogeosciences: Remote sensing.

Received 14 March 2008; **Revised** 20 May 2008; **Accepted** 9 June 2008; **Published** 19 August 2008.

Cakir, Z., and A. M. Akoglu (2008), Synthetic aperture radar interferometry observations of the M = 6.0 Orta earthquake of 6 June 2000 (NW Turkey): Reactivation of a listric fault, *Geochem. Geophys. Geosyst.*, *9*, Q08009, doi:10.1029/2008GC002031.

1. Introduction

[2] On 6 June 2000, less than a year after the devastating 1999 Izmit (M_w = 7.4) and Düzce (M_w = 7.2) shocks, a moderate-sized (M_w = 6.0) earthquake struck the town of Orta located ~130 km east of the eastern termination of the Düzce rupture near Bolu (Figure 1) [*Cakir et al.*, 2003a, 2003b]. Felt from the capital, Ankara (~70 km to the south), the earthquake caused minor property damage in the town of Orta and some villages to the west and gave rise to 3 human casualties with more than 200 injuries. The earthquake was somewhat surprising first because its epicenter is located in a region far (30–35 km southward) from the plate boundary, North Anatolian Fault (NAF), where no active faults were previously reported to exist. Second, the fault plane solutions show that the event is associated with an oblique-normal-slip fault trending at an high angle to the strike-slip NAF (Figure 2). Most of the focal mechanism solutions from various different sources are in good agreement and indicate an oblique normal displacement either on an eastward dipping (24°–54°) and north-south trending left-lateral strike-slip fault or on a westward dipping (59°–80°) and northwest–southeast trending right-lateral strike-slip fault (Table 1). However, field investigations following the earthquake did not reveal a clear fault rupture at the Earth's surface. Instead, some cracks, fissures and minor landslides were observed to have been caused by the earthquake [*Emre et al.*, 2000; *Kocyigit et al.*, 2001]. Running through the village of Dodurga, most of these fractures apparently fall in a narrow zone that is approximately 10-km-long and trends roughly in the north-south direction (Figure 2) [*Emre et al.*, 2000]. In addition, some of the fractures with a north-south strike appear to display left-lateral sense of slip, in agreement with the focal mechanism solutions. Taking into account these observations and the subsequent fault mapping based on aerial photography and field observations, *Emre et al.* [2000] concluded that the earthquake must have taken place on a north-south trending left-lateral fault that they later named as the Dodurga fault. Considering the distribution of the surface cracks and the foreshocks and aftershocks, and their new fault map shown in Figure 2, *Kocyigit et al.* [2001] supported the inference of *Emre et al.* [2000] that the event is most probably due to the reactivation of the Dodurga fault. Teleseismic waveform inversions by *Utkucu et al.* [2003] and *Taymaz et al.* [2007] indicate up to 2.3 m of oblique slip centered around 5–6 km of depth on a moderately dipping fault (46–47°).

[3] Previous earthquakes have shown that such surface cracks and fissures observed in the field should be interpreted with caution since they may not necessarily indicate the location of the causative fault of the earthquake [e.g., *Akoglu et al.*, 2006; *Cakir et al.*, 2006; *Talebian et al.*, 2004]. Therefore, the kinematics, location and geometry of the ruptured fault are still open to question owing to the absence of a clear surface rupture and a precise determination of aftershock locations. The objective of this study is thus to provide better constraints on the kinematics, fault geometry and the rupture parameters of the 6 June 2000 Orta earthquake using synthetic aperture radar (SAR) data.

[4] We map the coseismic surface deformation field of the earthquake using synthetic aperture radar interferometry (InSAR) with the European Space Agency's ERS-2 satellite data. We then model the coseismic interferograms using elastic dislocations on rectangular faults with a nonlinear inversion procedure. *Taymaz et al.* [2007] also deduce fault parameters by inverting separately one of the coseismic interferograms of the earthquake we used in this study. However, they do not discuss or reconcile the discrepancy between their modeling results and field observations. Here, we analyze together with the field observations two additional and independent coseismic interferograms that enable us to interpret the surface deformation field and deduce the rupture characteristics with more confidence and in more detail. We also use the modeling results to interpret the active tectonics of the region, and finally discuss the pitfalls and shortcomings in determining the source parameters of earthquakes on the basis of field

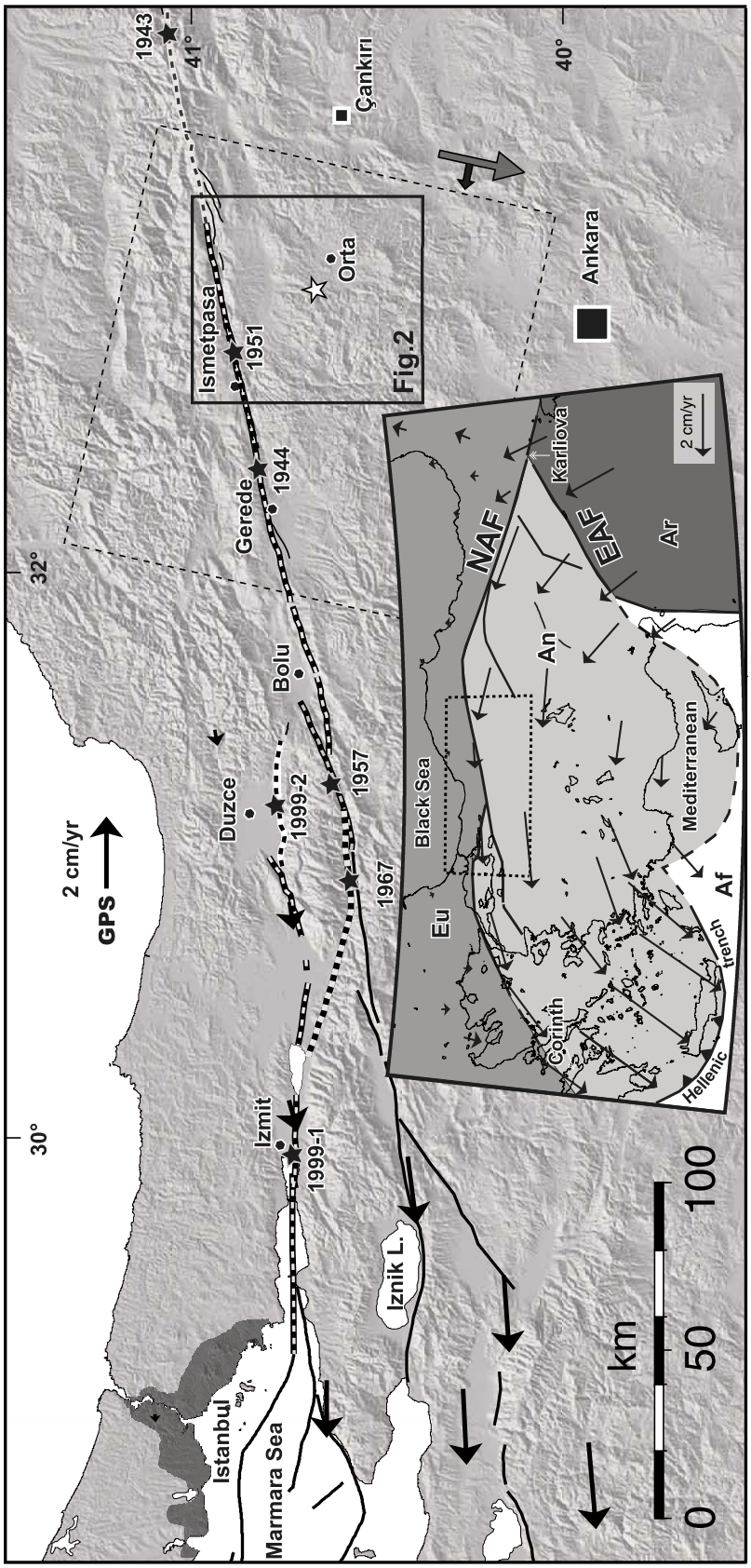
1943
41°
Çankırı
40°
Ankara
Orta
Fig.2
Ismetpasa
1951
Gerede
1944
32°
Bolu
Duzce
1999-2
1957
1967
2 cm/yr
GPS
30°
Izmit
1999-1
Iznik L.
Istanbul
Marmara Sea
km
0
50
100
NAF
EAF
Ar
An
Eu
Af
Black Sea
Mediterranean
Kariiova
2 cm/yr
Corinth
Hellenic
trench

Figure 1

observations, seismicity and InSAR data when faulting does not reach to the surface.

2. Seismotectonic Setting

[5] The main neotectonic structure of the study area is the North Anatolian Fault (Figure 1). The epicentral area of the Orta earthquake of 6 June 2000 is located 30–35 km south of the Ismetpasa creeping section of the NAF (Figures 1 and 2) [*Cakir et al.*, 2005]. Extending for over 1500 km from the Karliova triple junction in eastern Turkey to the Corinth Rift in central Greece, the right-lateral NAF is one of the most prominent and seismically active structures of the Eastern Mediterranean region (Figure 1) [*Armijo et al.*, 1999; *Barka*, 1996; *Sengör et al.*, 2005]. It accommodates, along with its conjugate left-lateral East Anatolian Fault (EAF), the westward extrusion of the Anatolian plate resulting from the collision between the Arabian and Eurasian plates in late Miocene [*Sengör et al.*, 1985]. In central north of Turkey, it follows an arc nearly parallel to, and about 100 km from, the Black Sea coast between Karliova and Bolu, enabling the contour clock wise rotation of the Anatolian plate about a pole located in Sinai (Egypt) with a slip rate of about 2.4 cm/a (Figure 1) [*McClusky et al.*, 2003; *Reilinger et al.*, 2006]. However, the circle arc of the Anatolian plate rotation does not quite coincide with the trace of the NAF; while the plate motion is almost parallel to the NAF along the NW-SE trending portion of the arc in the east, imposing pure strike-slip motion on it, it is slightly oblique along its NE-SW trending section in the earthquake area to the west, promoting a minor thrust-slip component that is, according to the field observations [*Hubert-Ferrari et al.*, 2002], taken up by secondary thrust faults [*Flerit et al.*, 2003; *McClusky et al.*, 2000]. Field evidence suggests that strike-slip deformation in this section of the NAF (i.e., north-central Turkey) is highly localized with large earthquakes occurring on the same fault segments over many seismic cycles [*Kozaci et al.*, 2007]. To the west of Bolu, the NAF is no longer a simple and single structure but, splits into several branches where the strike-slip regime becomes overwhelmingly transtensional [*Armijo et al.*, 2002].

[6] While the NAF and EAF have attracted interest of many researchers because of the high rate of recent and historical seismic activity and the presence of conspicuous morphotectonic features associated with active faulting along them, little attention has so far been paid to the secondary active faults around them. Therefore, no active faults were reported to have been present in the Orta region before the earthquake nor does the Active Fault Map of Turkey [*Saroglu et al.*, 1992] include the causative fault of the Orta event (Figure 1). Some secondary fault strands splaying from the NAF to the south are reported to be present east of the earthquake area [*Bozkurt*, 2001; *Kocyigit et al.*, 2001]. But no active faults of north-south trend were reported before the Orta earthquake. Neotectonic map of the epicentral area and the surrounding regions is done by *Kocyigit et al.* [2001] shortly after the earthquake (Figure 2). In the earthquake area, they mapped in detail the Dodurga fault claimed by *Emre et al.* [2000] to have ruptured during the Orta earthquake. They proposed that it is not a single structure but, comprises closely spaced (a few kilometers) and N–S trending sub parallel strike-slip faults with significant normal component (Figure 2). In addition, their map shows numerous other faults around the epicentral region. However, as can be seen in Figure 2, most of these faults do not have any morphological expression visible in the topography at a resolution of 90 m (i.e., the SRTM digital elevation data), suggesting that most of the lineaments seen in the aerial or satellite imagery are inactive faults or have very low Quaternary activity, or of possibly non-tectonic origin.

[7] The NAF experienced a well-known sequence of westward migrating earthquakes in the last century between 1939 and 1999, three of which

Figure 1. Tectonic map of northwestern Turkey showing the active faults (solid black lines) [*Saroglu et al.*, 1992; *Armijo et al.*, 2002], 20th century earthquake fault ruptures (two-color thick dashed lines with dates and black stars) along the North Anatolian fault, and the location of the study area (box with solid lines) over shaded relief image produced from the Shuttle Radar Topography Mission (SRTM) 90-m-posting elevation data. Dashed box is the ERS SAR data frame (frame 2781 of track 479). The gray and black arrows attached together show the satellite flight direction (descending) and the line of sight direction (right looking), respectively. Epicenter of the earthquake of 6 June 2000 is shown with a white star. Inset map depicts the configuration of tectonic plates (Eu, Eurasia; Af, Africa; Ar, Arabia; An, Anatolia) in the eastern Mediterranean region with GPS vectors [from *McClusky et al.*, 2000] showing westward motion of the Anatolian block relative to the Eurasian plate via the right-lateral North Anatolian fault (NAF) and the left-lateral East Anatolian fault (EAF).

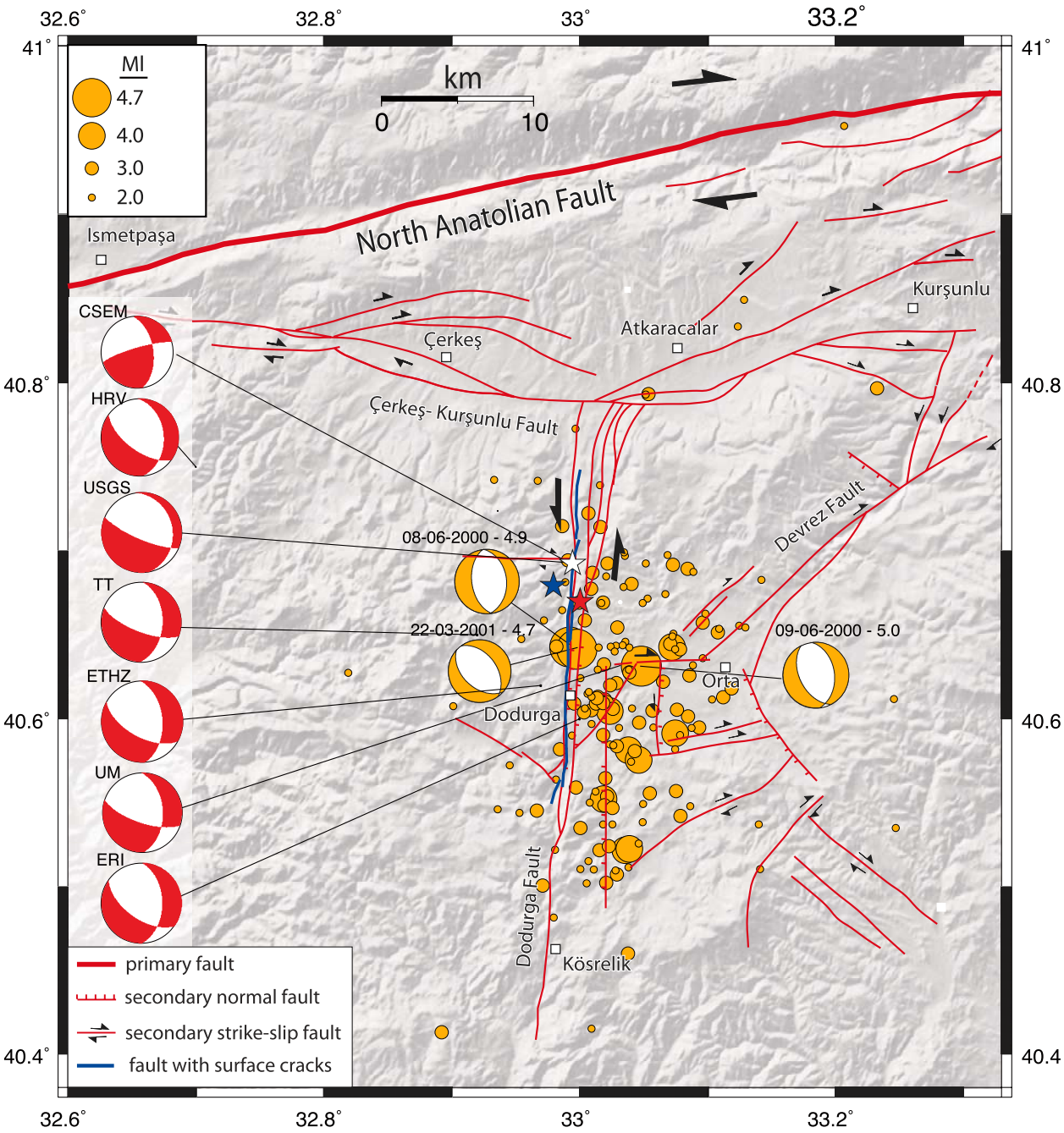

Figure 2. Active fault map of the Orta region from *Kocyigit et al.* [2001], *Emre et al.* [2000], and *Saroglu et al.* [1992]. Blue line is the Dodurga fault along which some cracks and fissures were observed and claimed by *Emre et al.* [2000] to be the fault responsible for the Orta earthquake (see Table 1). Red beach balls are focal mechanism solutions of the main shock from various sources. Red, blue, and white stars mark the epicenter of the earthquake of June 2000 estimated by the Earthquake Research Department of the General Directorate of Disaster Affairs (ERD), Kandilli Observatory, and USGS, respectively. Yellow circles are the aftershocks recorded by ERD during six months following the main shock with focal mechanisms (yellow beach balls) from ETHZ. North-south elongation of aftershocks suggests that the nodal plane dipping to the east is most likely the one that represents the fault rupture, an inference also being supported by their concentration on the eastern side of the Dodurga fault.

Table 1. Fault Plane Solutions of the Orta Earthquake of 6 June 2000 Estimated by Various Institutions, Researchers, and This Study

			Nodal plane 1			Nodal plane 2							
Lon. (°E)	Lat. (°N)	D. (km)	Str. (°)	Dip (°)	Rake (°)	Str. (°)	Dip (°)	Rake (°)	M_o (10^{18} N.m.)	Slip (cm)	Length (km)	RMS (mm)	Source[a]
32.992	40.693	3.00	349	24	−37	113	76	−110	1.3	–	–	–	USGS
–	–	10.00	352	54	13	254	80	143	0.8	–	–	–	CSEM
32.700	40.750	15.00	356	39	−47	126	62	−119	1.1	–	–	–	HRV
32.970	40.620	15.00	356	49	−44	119	59	−129	1.4	–	–	–	ETHZ
33.000	40.600	33.00	360	48	−47	125	58	−126	1.3	–	–	–	ERI
33.030	40.630	5.00	358	47	−30	109	69	−133	1.0	42	–	–	UM
32.980	40.700	3.0–9.0	002	46	−29	113	70	−132	1.4	111	7	–	TT-waveform
32.960	40.630	3.2–7.7	001	59	−23	103	70	−147	1.5	100[b]	9	–	TT-sar
32.923[c]	40.613	4.5–5.8	348	34	−47	120	66	−115	1.16	127	11.3	6.6	SAR 1-fault
32.928[c]	40.632	3.6–6.5	2[b]	33	−38	125	70	−117	1.31	72	10.4	9.3	SAR 1-fault
32.922[c]	40.633	4.0–6.6	2[b]	33	−37	122	70	−121	1.38	78	10	8.7	SAR 2-fault
32.988[c]	40.626	0.0–2.5	2[b]	83	−18	–	–	–		5	19.3		

[a] USGS, U.S. Geological Survey; CSEM, European-Mediterranean Seismological Centre; HRV, Harvard; ETHZ, Eidgenössische Technische Hochschule Zürich; ERI, Earthquake Research Institute, Tokyo; TT, *Taymaz et al.* [2007]; UM, *Utkucu et al.* [2003]; SAR, this study).
[b] Parameter is fixed.
[c] Center of the fault projected updip to the surface.

ruptured, with surface breaks, the NAF in the vicinity of the Orta earthquake region; the 1943 (M_w 7.6), 1944 (M_w 7.3) and 1951 (M_w 6.9) earthquakes (Figure 1) [*Toksöz et al.*, 1979]. Kandilli Observatory, Earthquake Research Department of the General Directorate of Disaster Affairs (ERD) and the United States Geological Survey located the epicenter of the 6 June 2000 earthquake at about 10 km northwest of the town of Orta, roughly on the central part of the Dodurga fault (stars in Figure 2). The earthquake was not a total surprise because the region had been seismically active quite for some time. The seismic activity started one and a half years before the main shock during which ∼272 foreshocks of magnitudes reaching up to 4.9 were recorded by the Earthquake Research Institute of General Directorate of Disaster Affairs (Figure 3b). Interestingly, seismicity vanished dramatically after the 1999 Izmit and Düzce earthquakes (Figure 3a); only a few earthquakes occurring during the last 7–8 months before the main shock. It is unlikely that the fading seismicity and the following seismic quiescence before the Orta main shock are associated with Coulomb stress transfer from these earthquakes since our calculations indicate that the static stress increase for N–S trending oblique normal faults is only about 0.04 bars in the Orta region. It may have been due to aseismic creep on the Dodurga fault triggered by dynamic stresses caused by the passage of seismic waves of the 1999 earthquakes or the temporal behavior of pre-earthquake activity during these previous events may simply be coincidental.

[8] About 140 aftershocks took place within six months following the earthquake. Of these, ten are larger than magnitude 4. The largest one was an M = 5 normal event, and occurred ∼5 km southeast of the main event three days later. Focal mechanism solutions of two other large aftershocks also indicate nearly pure normal faulting (Figure 2). Aftershocks were not recorded by a local network and thus were not precisely located. Nevertheless, similar to the foreshocks (Figure 3b), most of them are concentrated on the eastern side of the Dodurga fault and are distributed roughly in north-south direction, suggesting that the earthquake is indeed associated with a north-south trending and eastward dipping fault in agreement with focal mechanism solutions (Figure 2 and Table 1).

3. Surface Deformation Field From InSAR

[9] The InSAR technique consists of combining radar images of the same area acquired at different times to extract the interferometric phase, which gives a measure of the radar-to-ground path difference between the two images. After removing the phase contributed by topography and orbital separation, the interferometric phase represents the line of sight (LOS) component of the surface displacement that occurred during the time interval covered by the two images [*Gabriel et al.*, 1989].

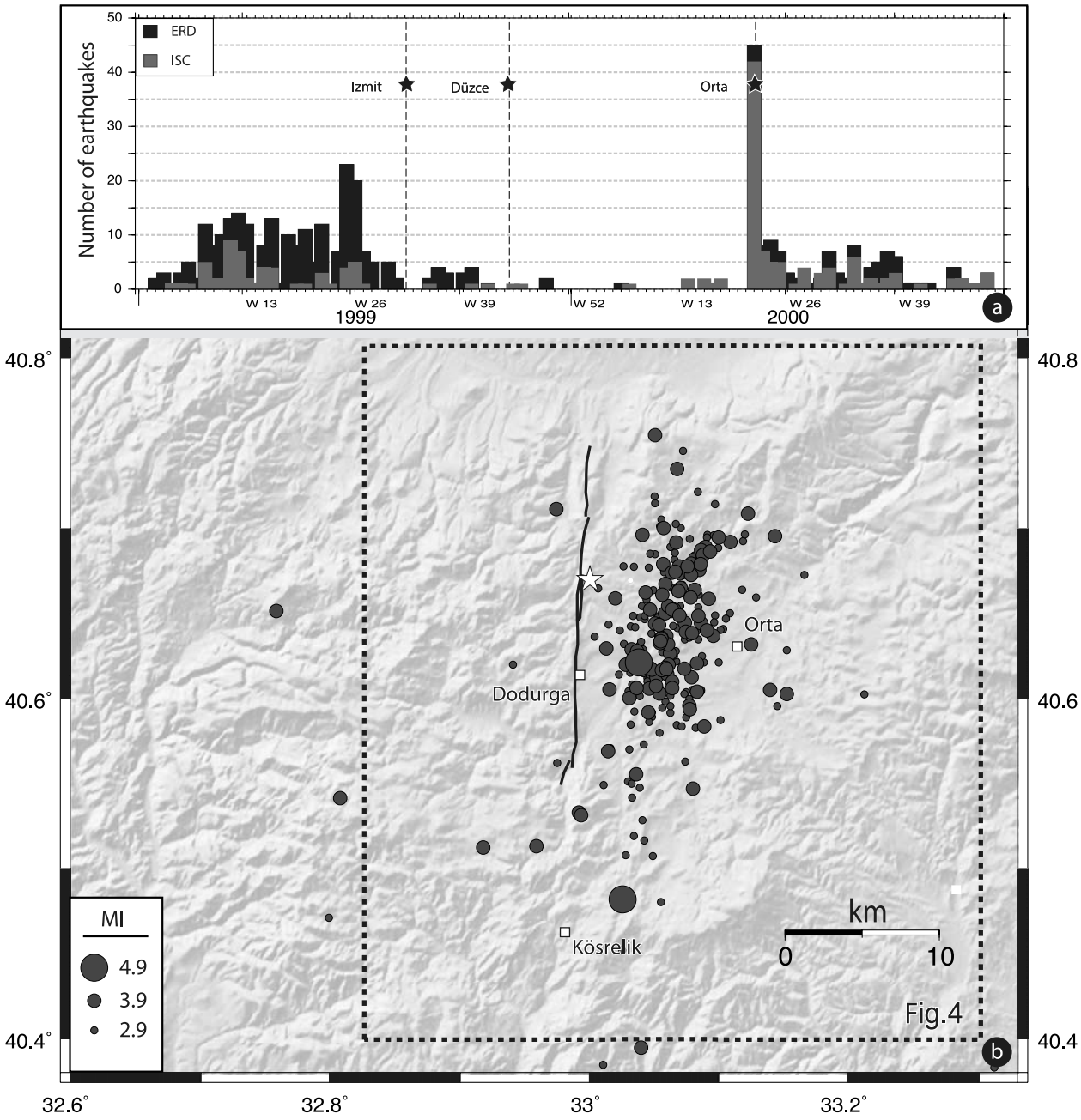

Figure 3. (a) Seismicity in the Orta region (32.7°–33.3°E, 40.4°–40.85°N) before and after the main shock between January 1999 and December 2000 based on the catalogs of ERD and the International Seismological Center (ISC). Lasting about 8 months as from the beginning of the year 1999, an earthquake storm occurred in the epicentral area. The seismic activity interestingly ceased after the 1999 Izmit and Düzce earthquakes. The quiescence was, however, broken by the Orta earthquake about 8–10 months later. (b) Distribution of foreshocks between January 1999 and June 2000. Note that like the aftershocks, seismic activity before the main shock is concentrated to the east of the Dodurga fault (black lines) and distributed roughly in the north-south direction, supporting the inference that it is this fault that ruptured during the earthquake. Dashed rectangle is the area of Figure 4.

Since its application to the 1992 Landers earthquake [*Massonnet et al.*, 1993], the technique has been widely used to study crustal deformation resulting from the earthquake cycle [*Bürgmann et al.*, 2000; *Massonnet and Feigl*, 1998; *Wright et al.*, 2001b; *Zebker et al.*, 1994]. The main error on LOS range change estimates is often due to varia-

Table 2. Coseismic Pairs of SAR Images From the Descending Orbit of the ERS Satellites That Are Processed in This Study[a]

		Master			Slave					
Int.	Number	Sat	Orbit 1	Date 1[b]	Sat	Orbit 2	Date 2	$B_\perp$ (m)	H_a (m)	Δ Date
Int-1	1	ERS2	22878	05/09/1999	ERS2	26886	11/06/2000	−67	148	280
Int-2	2	ERS2	22377	01/08/1999	ERS2	28890	29/10/2000	158	63	455
Int-3	3	ERS2	7848	20/10/1996	ERS2	38910	29/09/2002	79	127	2170
Int-4	4	ERS2	23379	10/10/1999	ERS2	38409	25/08/2002	−222	45.2	1050
Int-5	5	ERS2	22377	01/08/1999	ERS2	33900	14/10/2001	−324	31	805
Int-6	6	ERS2	22377	01/08/1999	ERS2	37908	21/07/2002	131	76.7	1085
Int-7	7	ERS2	22377	01/08/1999	ERS2	43419	10/08/2003	191	52.6	1470
Int-8	8	ERS2	22377	01/08/1999	ERS2	44421	19/10/2003	−92	109	1540
Int-9	9	ERS2	7848	20/10/1996	ERS2	43920	14/09/2003	−60	167	2520
Int-10	10	ERS1	22010	30/09/1995	ERS2	33900	14/10/2001	−282	35.6	2206
Int-11	11	ERS1	21008	22/07/1995	ERS2	28890	29/10/2000	39.8	252	1926
Int-12	12	ERS2	1335	23/07/1995	ERS2	28890	29/10/2000	−4.6	2185	1925
Int-13	13	ERS1	4632	04/06/1992	ERS2	33900	14/10/2001	−344	29	3419
Int-14	14	ERS1	21509	26/08/1995	ERS2	42417	01/06/2003	33.2	302	2836
Int-15	15	ERS2	1335	23/07/1995	ERS2	27888	20/08/2000	33.6	299	1855
Int-16	16	ERS2	21876	27/06/1999	ERS2	38910	29/09/2002	−153	−65.6	1190

[a] Track: 479; Frame: 2781. Interferograms Int-1, Int-2, and Int-3 are those shown in Figure 4. $B_\perp$, perpendicular baseline (m); H_a, altitude of ambiguity (m).
[b] Read 05/09/1999 as 5 September 1999.

tions in the phase propagation delay through the troposphere [*Hanssen*, 2001; *Zebker et al.*, 1997].

[10] In order to examine the ground displacements resulting from the Orta earthquake of 6 June 2000, we produced many coseismic interferograms using SAR data acquired by ERS satellites (wavelength 5.6 cm) from descending orbits (radar looking toward west; Figure 1) (Track: 479; Frame: 2781) (Table 2). Descending SAR images are the only geodetic data available for this earthquake; there are no GPS points nearby or suitable pairs from the ascending orbits in the ERS SAR catalog. The raw data are processed using JPL's (NASA) Roipac software (version 2.2.2) [*Rosen et al.*, 2004] and precise satellite orbits from Delft University [*Scharroo and Visser*, 1998]. The Delft orbits were found to be satisfactory and thus no orbital adjustment is made in the interferograms. Contribution of topography is simulated and removed from the interferograms using the Shuttle Radar Topography Mission (SRTM) 3-arc-second posting digital elevation model [*Farr et al.*, 2007].

[11] Figure 4 shows the best three interferograms that are filtered using a weighted power spectrum technique [*Goldstein and Werner*, 1998]. Each fringe, that is, one cycle of phase difference (e.g., from blue to blue) in the interferograms, corresponds to a range change of 2.83 cm along line of sight (LOS) between the radar and the Earth's surface. Coherence in the interferograms decreases with increasing temporal baseline (i.e., time lapse between the image acquisitions) but, is well preserved even in the interferogram spanning 6 years (Int-3; Figure 4c and Table 2). This is owing to sparse vegetation cover and limited agricultural activity in this region of arid climate, which allowed us earlier to study the creeping phenomenon along the Ismetpasa section of the NAF to the north using long-term SAR interferometry [*Cakir et al.*, 2005]. The high signal correlation is also partly owing to the fairly flat topography of the region where most of the deformation fringes are located (Figure 3d). Although temporal decorrelation increases to the west of the Dodurga fault in the hilly areas where the topographic elevation increases ~350 m in a very short distance, some closely spaced fringes are still visible as a result of the high altitude of ambiguity (sensitivity of the interferograms to the topography) of interferograms (Table 2). These fringes may partly contain atmospheric noise correlated with topography.

[12] All the interferograms are independent from each other; that is, they do not share a common master or slave image (Table 2). This allows us to better evaluate atmospheric effects and have high degree of confidence in our interpretation of fringes. As may also be seen from Figure 4, subtracting interferograms from one another shows that the difference between them is small and thus

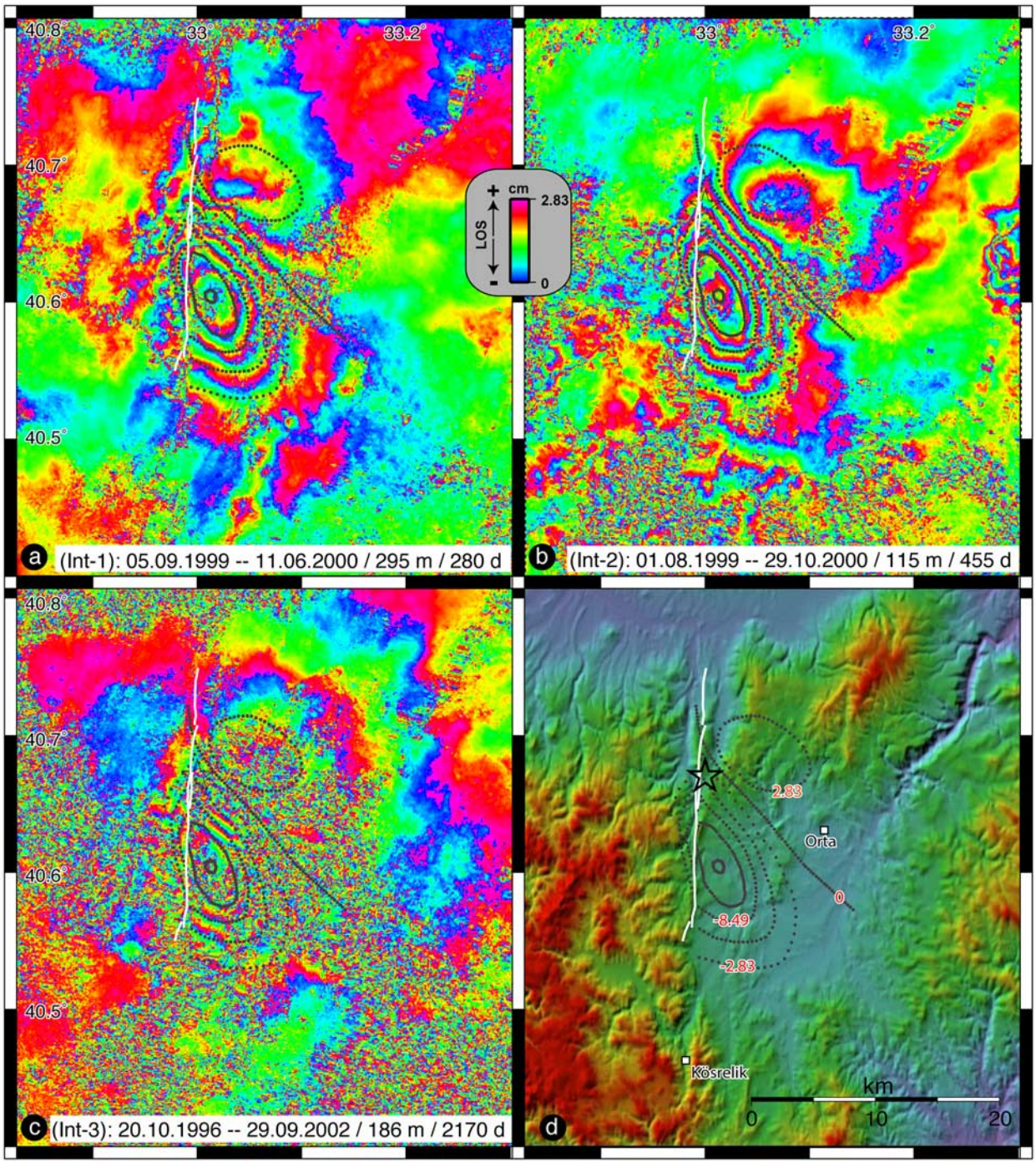

Figure 4. (a–c) Three independent coseismic interferograms (Int-1, Int-2, Int-3) of the Orta earthquake of 6 June 2000. Date of the orbit pairs, altitude of ambiguity (m), and temporal baselines (time difference in day between the acquisitions of the two images) are given in white boxes at the bottom of the interferograms. Each fringe (a full color cycle) shows half a wavelength range change (i.e., 2.83 cm) between the radar and Earth's surface. The unit vector along the range is 0.35, −0.088, 0.92 in east-north-up coordinates. White dashed line is the surface trace of the Dodurga fault. Star marks the earthquake epicenter determined by ERD. Dotted lines show the digitized fringes of Int-2 (southern lobe) and Int-3 (northern lobe) used in the inversion. (d) Shaded SRTM relief image of the epicentral region. Note that the Dodurga fault crosscuts the fringes in the northern side of the teardrop-shaped fringe lobe.

they do not contain any significant atmospheric artifacts. One of the interferograms (Int-2) spans a postseismic period of ~4.5 months and the other (Int-3) ~2 years. Comparison of the interferograms also reveals that the postseismic deformation must be in the noise level of the interferograms. The main fringe pattern in all of the interferograms is a teardrop-shaped lobe of up to 15 cm (~5 fringes) of range increase with a northward pointing cusp and a NW–SE trending long axis (Figure 4). Following *Amelung and Bell* [2003], we refer to this fringe pattern as the teardrop feature. In all the interferograms there is also a second but, much smaller fringe lobe of circular shape to the north of the teardrop feature. Although its shape, location and amplitude slightly vary from one interferogram to the other, it shows an area of up to 5 cm range decrease. The most likely and reasonable explanation for the cusp seen in the fringe pattern of all the interferograms is the presence of a nearby fault rupture. Continuity of the fringes around the cusp suggests that the rupture did not quite reach to the surface. The first fringe in the south, however, abuts the fault and do not seem to continue on the western side of the fault, implying that the faulting might have indeed reached to the surface along this part of the fault as suggested by *Emre et al.* [2000].

4. Source Model of the Orta Earthquake

[13] We model the interferograms in an inverse approach using dislocations with uniform slip in a homogenous and elastic half-space. To perform the inversions, we employ a residual-minimization procedure based on a downhill simplex simulated annealing algorithm [*Donnellan and Lyzenga*, 1998]. A χ^2 goodness of fit objective function is formed from SAR data set and its measurement uncertainties. Function evaluations are based on the analytical solutions for rectangular dislocations in a homogenous half-space given by *Okada* [1985]. Simulated annealing parameter estimation process is able to locate the global objective function minimum by climbing out of local minima. For the inversions, we use digitized fringes instead of unwrapped data since some parts of the teardrop feature cannot be properly unwrapped owing to the temporal decorrelation (Figure 4). This also allows us to reduce the large amount of SAR data down to about 400 data points and hence expedite the modeling process. We sample the interferograms in such a way that data spacing increases from the edge to the center of the teardrop feature, which is, to some extent, similar to the quadtree sampling of unwrapped interferograms [*Jònsson et al.*, 2002]. Since the interferograms are quite similar, in our inversions we use only one set of fringe data that represents best all the three interferograms, instead of different sets of fringes for each one. The zero fringe is inferred on the basis of the phase color in between and/or around the two lobes, which is plotted with green color in the interferograms (Figures 4a–4c). Nine fault parameters can be solved by the inversion; longitude, latitude, strike, dip, depth, width, length, strike-slip and dip-slip. Although orbital residuals are not taken in to account in the inversions, visual inspection of the interferograms confirms that none of them contain orbital residuals more than one fringe at the scale of the interferogram (i.e., ~100 × 100 km). Therefore, bias in the fault parameters introduced by orbital residuals should be negligible.

[14] In the first stage of modeling, we invert all the parameters except the fault dip. Inversions with a fixed fault dip ranging between 20° and 70° show that the best fit model has an RMS misfit of 6.6 mm and is obtained with 127 cm of oblique left-lateral slip on a ~11-km long fault dipping 34° toward the east and striking 348° (i.e., N12°W) (Figure 5a). Although the strike of the best fit fault is not in disagreement with all of those determined from seismology (Table 1), it contradicts with the field observations since it crosscuts the Dodurga fault and a fault with such a NNW–SSE trend does not seem to exist in the epicentral area (Figure 6). Therefore, in the second stage of modeling, we invert the fault parameters keeping also the fault strike fixed at ~2°, that is, parallel to the strike of the southern section of the Dodurga fault that ruptured during the earthquake. Except some increase in RMS misfit (~40%), what essentially changes regarding with the best fit model when the fault strike is held fixed is the decrease in the fault rake from −47° to −38° (Figure 5b and Table 1). Almost all the modeled faults with various dip angles are now located on the eastern side of the Dodurga fault (Figure 6). The best fit to the SAR data in both modeling steps is obtained with faults with rather low dip angles (33°–34°), in agreement with the seismological estimates (e.g., USGS and Harvard solutions; Table 1). Such low-angle faults are known to exist elsewhere but, are normally associated with pure dip-slip normal faulting that may be facilitated by the presence of unusually high pore fluid pressure on a preexisting plane of weakness or rotation of the stress field at the

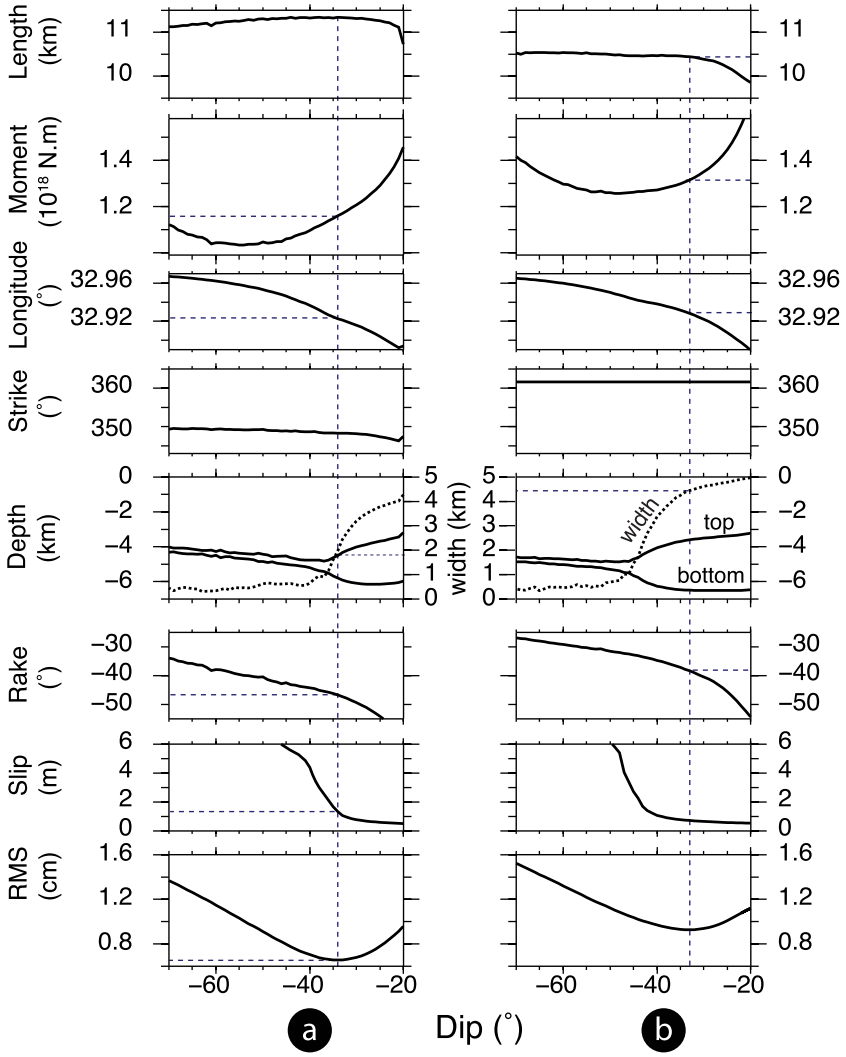

Figure 5. Plots showing the variation of fault parameters and root mean square (RMS) misfit with a fixed fault dip between 20° and 70° when the SAR data set is inverted (a) keeping all the other parameters free or (b) holding also the fault strike fixed. The best fit with the free inversion has a 6.6 mm of RMS misfit and is obtained with a fault dipping 34° to the east. When the fault strike is kept fixed at N2°E parallel to the strike of the Dodurga fault, most of the model parameters remains essentially the same. Faulting is now dominantly strike-slip (−38° of rake). Dashed lines are drawn for a better visualization of the parameters predicted by the best fitting models.

hypocentral depth within the brittle layer [*Bernard et al.*, 1997; *Westaway*, 1999]. Thus, the dominant strike slip component of this earthquake makes it interesting and is somewhat similar to the Düzce earthquake that took place on a surprisingly low angle (∼60°) fault with nearly pure strike-slip displacement [*Bürgmann et al.*, 2002; *Cakir et al.*, 2003a].

[15] As also noted by *Taymaz et al.* [2007] there are tradeoffs between several fault parameters. For example, as seen in Figure 5, dip angle tradeoffs with slip and also with rake such that slip decreases with dip. Thus, one parameter must be known or held fixed at a value consistent with some fault scaling laws [e.g., *Wells and Coppersmith*, 1994] to constrain the other one. The upper boundary for an acceptable fault dip can be constrained by the amount of slip and the width of the fault. With increasing amount of dip, while the fault width gets thinner and thinner becoming less than half a kilometer, the slip reaches over 5–6 m above 40°–45° (Figure 5b). Therefore, faults dipping above 45° have unusual aspect ratios and predict abnormally high coseismic slip for an earthquake of magnitude 6 [e.g., *Wells and Coppersmith*,

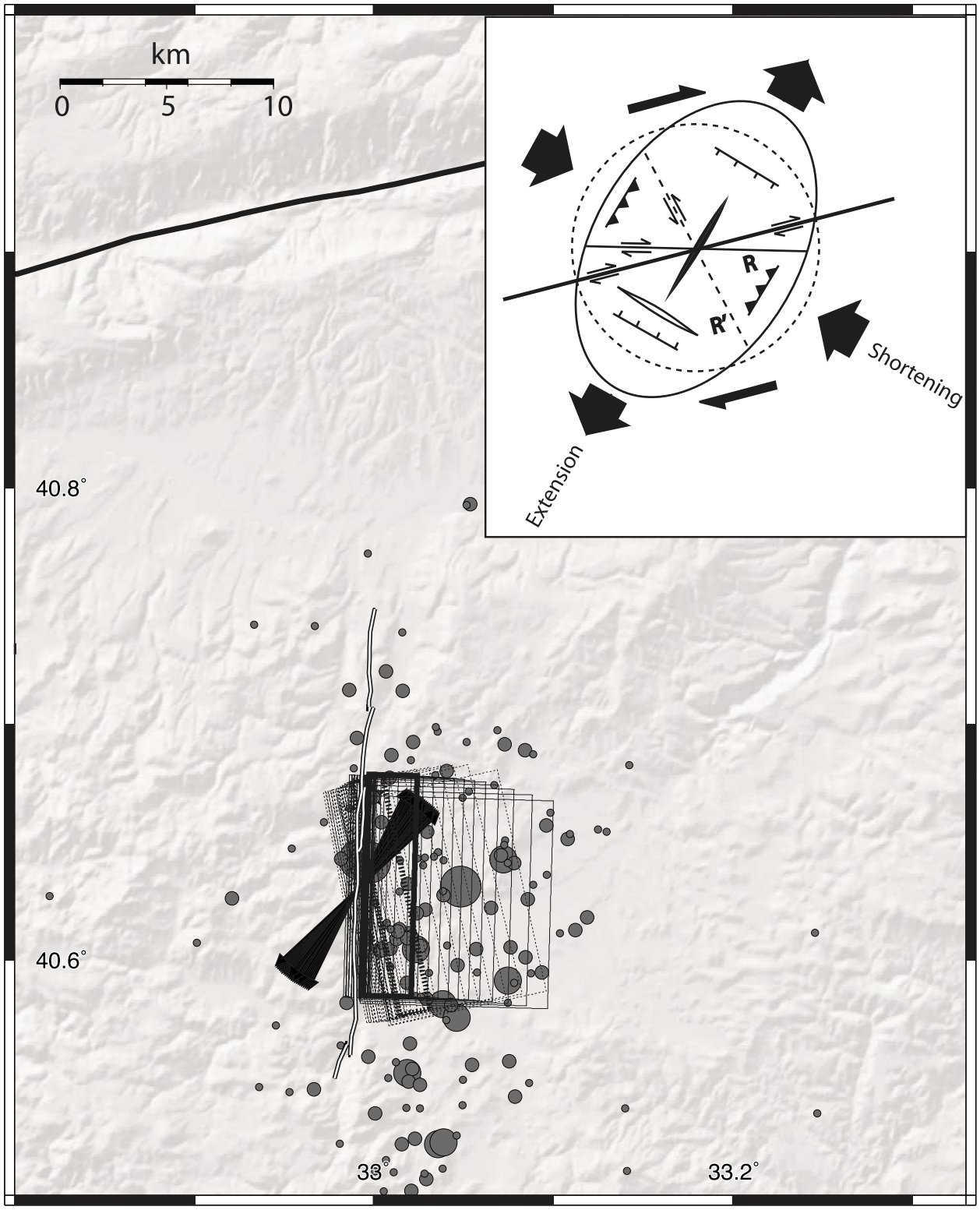

Figure 6

1994]. Despite such tradeoffs, some parameters like, the length, location, depth range of faulting and moment, are well determined (Figure 5).

[16] Figure 7a shows the synthetic interferogram obtained by projecting to the satellite the 3-D surface deformation predicted by the best fitting model with a fault striking N2°E. Overall fringe pattern of the observed interferograms are well reproduced by the model. The excellent fit between the model and data is demonstrated by the residual interferograms plotted in Figures 7b and 7c. Model fault parameters, including the geodetic moment, are also in good agreement with seismological observations (Table 1). However, the relationship between the modeled fault at depth and those mapped at surface is not quite obvious and thus requires some explanation. As illustrated in the map and the cross-section plotted in Figure 7a, the surface trace of the best fit fault will be located 4–5 km west of the Dodurga fault if it is projected up dip to the surface (white dashed line in the map and in the inset profile). Otherwise, the modeled fault will require a sharp decrease in the dip angle if it is to be connected to the Dodurga fault at surface (blue line in the inset profile). Arranged in a configuration similar to that illustrated in the profile shown in Figure 7a, the Dodurga fault might also have been reactivated together with its master fault as a synthetic fault. Therefore, the earthquake might have been associated with multiple ruptures similar to the 25 February 1981 Corinth event [*Jackson et al.*, 1982]. However, no such fault is mapped by *Emre et al.* [2000] or *Kocyigit et al.* [2001] (Figure 2) nor is its morphological expression present in the topography. Even if it exists, the rupture does not seem to reach to the surface because there is no apparent anomaly in any of the interferograms even though signal correlation is low west of the Dodurga fault. On the other hand, the SAR data clearly support the field observations that suggest that the Dodurga fault ruptured during the earthquake [*Emre et al.*, 2000]. Reactivation of the Dodurga fault with a small amount of slip is evident by the discontinuity of some fringes across the fault, and particularly by the presence of the cusp in the fringe pattern that cannot be otherwise explained by atmospheric artifacts since it exists in all the interferograms constructed from different orbits. In the absence of additional field observations, it follows that either the Dodurga fault has listric geometry or it cuts a preexisting low-angle surface (e.g., an old thrust plane) that was later reactivated during the earthquake. The accuracy of aftershock or foreshock depths are unfortunately inadequate to infer the fault geometry.

[17] In the third stage of modeling, we therefore use two rectangular faults in order to approximate roughly the geometry of a listric fault, one having a steep dip angle and coinciding with the Dodurga fault trace at the surface and the other having a low dip angle at deeper depths. Thus, fixing the strikes of the two faults at ~2° and the location of one of them along the surface trace of the Dodurga fault, we invert the remaining fault parameters. Inversion predicts several centimeters of oblique slip (~5 cm) on a ~19 km long, steep (83°) fault that reaches to the surface from about 3 km of depth (Table 1). The parameters of the other fault are nearly the same as those of the low-angle fault predicted by the best fit single-fault model with N2°E strike (Table 1). The increase in the goodness of fit in terms of RMS is, however, not quite significant since the interferograms and thus the inverted data set contain little information about the deformation on the western side of the Dodurga fault (Table 1). Nevertheless, as shown in Figure 8, the resemblance between the model and data becomes remarkable. The cusp in the teardrop feature is mimicked quite well by the model. Surface faulting with a small slip on the Dodurga fault also explains the fringe pattern in the southern side of the teardrop feature better. In fact, as predicted by the two-fault model, the first one or two fringes in the southern side of the interferograms do not continue to the west across the Dodurga fault (Figures 4a and 8a). This is because LOS components of the southwesterly horizontal (away from the satellite) and vertical

Figure 6. Map showing the surface projections of the rectangular dislocation planes predicted by the inversion with a fault dip ranging between 20° and 70° when the strike is being held free (dashed boxes) or kept fixed at 2° (solid boxes). Best fitting faults are shown with thicker lines. Note that when the strike is let free, the inversions predict NNW–SSE trending faults that crosscut the Dodurga fault to the north. Circles are aftershocks as in Figure 2. Black arrows are the T axes of the focal mechanism solutions calculated from all the models shown in Figure 5 with dip angles ranging between 30° and 70°. Inset shows a strain model explaining subsidiary structures along an active fault with a simple shear model. T axes orientation is subparallel to the direction of extension, suggesting that the Dodurga fault and the North Anatolian fault are the products of the same stress regime.

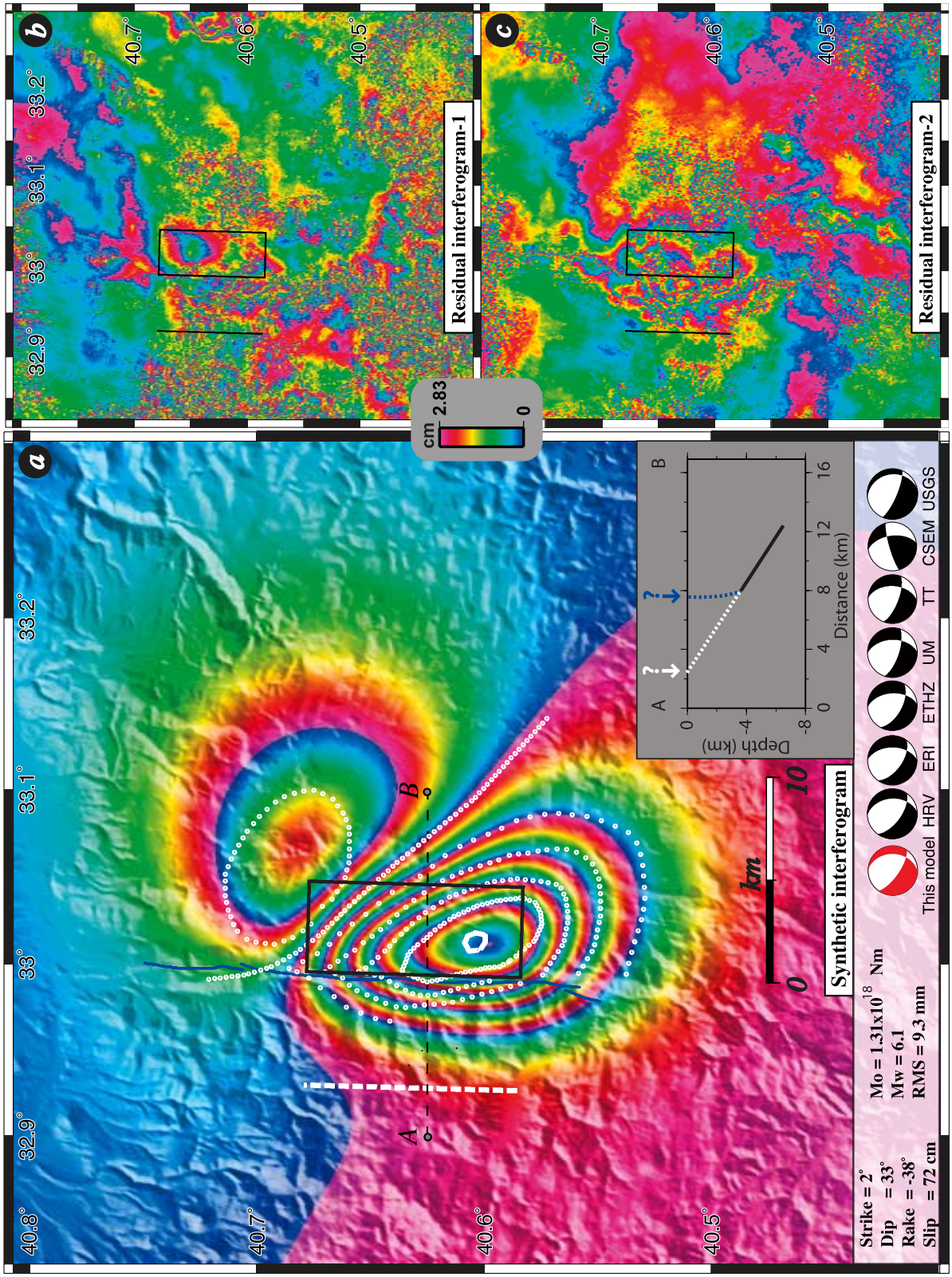
a
b
c
Residual interferogram-1
Residual interferogram-2
Synthetic interferogram
cm
2.83
0
km
10
Depth (km)
Distance (km)
A
B
Strike = 2°
Dip = 33°
Rake = -38°
Slip = 72 cm
Mo = 1.31x10^18 Nm
Mw = 6.1
RMS = 9.3 mm
This model HRV ERI ETHZ UM TT CSEM USGS

Figure 7

(uplift; toward the satellite) movements on the southwest quadrant of the deformation field of a NS trending, left-lateral strike slip fault cancel each other out, resulting in practically no phase difference. As mentioned above, continuity of the fringes around the cusp suggests that the rupture does not reach to the surface there. However, we do not think it is worthwhile to complicate the model further by introducing a third or even more patches to obtain a model with a variable slip distribution because the simple two-fault model provides quite a reasonable and satisfactory fit to the observed SAR data set, accounting for large majority of deformation fringes in the interferograms as illustrated by small residual phase in Figures 8b and 8c.

5. Discussion and Conclusions

[18] Careful analyses of multiple interferograms and modeling of InSAR data combined with field observations allow us to deduce that the earthquake was associated with a shallow (<6 km) left-lateral oblique normal displacement that occurred on a north-south striking, eastward dipping, listric fault. When it is not examined carefully as we initially did, the teardrop feature seems like a single compact lobe composed of closed polygonal fringes. Thus, one would normally expect the surface fault rupture to be located at the edge of this lobe, not crosscutting it. However, as Figure 4 shows, the Dodurga fault runs through the teardrop feature. This implies subsidence (i.e., range increase) on either side of the fault, which at first glance does not make sense, and consequently leads one to think that the Dodurga fault should not be directly blamed for the earthquake as implicitly suggested by *Taymaz et al.* [2007]. As shown in Figure 9, subsidence on the footwall block of a normal or oblique-normal fault does occur if the fault has listric geometry and the coseismic slip takes place essentially on its shallow dipping portions at depth. This would not be the case if the fault had planar geometry.

[19] The parameters of the gentler dipping, deeper fault are in good agreement with those deduced by *Taymaz et al.* [2007] from the interferogram Int-1 (Figure 4a) and seismic waveform modeling. Their InSAR-based model, however, predicts much steeper fault dip and higher seismic moment (Table 1). Although with a much higher RMS fit, interferograms may also be explained, to some extent, with right-lateral faulting (Figure 10) and one can reasonably attribute the anomalies in the fringe pattern resulting from near surface slip on the Dodurga fault to atmospheric artifacts. This implies that interpretation of the rupture characteristics of an earthquake based on a single interferogram may thus be misleading because even the determination of the fault mechanism may not be possible with a noisy interferogram, especially when the evidence of surface faulting in the field is not quite clear. It follows that field observations provide an essential piece of information in constraining fault parameters using geodetic data and that the use of multiple interferograms, if possible, is necessary to discriminate surface deformation from atmospheric effects [*Massonnet and Feigl*, 1998].

[20] The minor slip on the steep shallow fault may have taken place at the same time or nearly simultaneously with the main rupture on the low-angle fault or afterward as triggered seismic or aseismic shallow afterslip [*Fielding et al.*, 2004; *Freed et al.*, 2006; *Wright et al.*, 2001a]. Observation of the surface cracks several hours after the main shock (Ö. Emre, personal communication, 2008) suggests that it happened most probably during the main shock or immediately after as

Figure 7. (a) Synthetic interferogram predicted by the best fitting single-fault model with a N2°E strike, 33° eastward dip, and −38° rake (left-lateral with normal component). Moment (M_o), moment magnitude (M_w), and the RMS misfit values are indicated at the bottom (see Figure 5b and Table 1 for other parameters). Digitized fringes (dotted lines) used in the inversion are shown for visual comparison between the observed and modeled fringes. Also shown for comparison are the focal mechanism solutions determined from seismology (black beach balls) and from this model (red beach ball). Bold black rectangle is the surface projection of the ~10-km-long modeled fault located at a depth between 3.6 and 6.5 km. North-south trending white bold dashed line is the updip projection of the model fault to the surface which is located about 5 km west of the surface trace of the Dodurga fault (blue lines) as illustrated in the inset box with a vertical cross section. This suggests that if the Dodurga fault ruptured during the earthquake, it must have listric geometry or connect to a master fault at depth that reaches to the surface west of the Dodurga fault as illustrated in the inset box. (b and c) Residual interferograms obtained by subtracting the synthetic interferogram from the best two interferograms shown in Figures 4a and 4b. Small residual fringes illustrate that the model successfully predicts the observed interferograms. The remaining fringes are mostly atmospheric noise that is apparent outside the earthquake area.

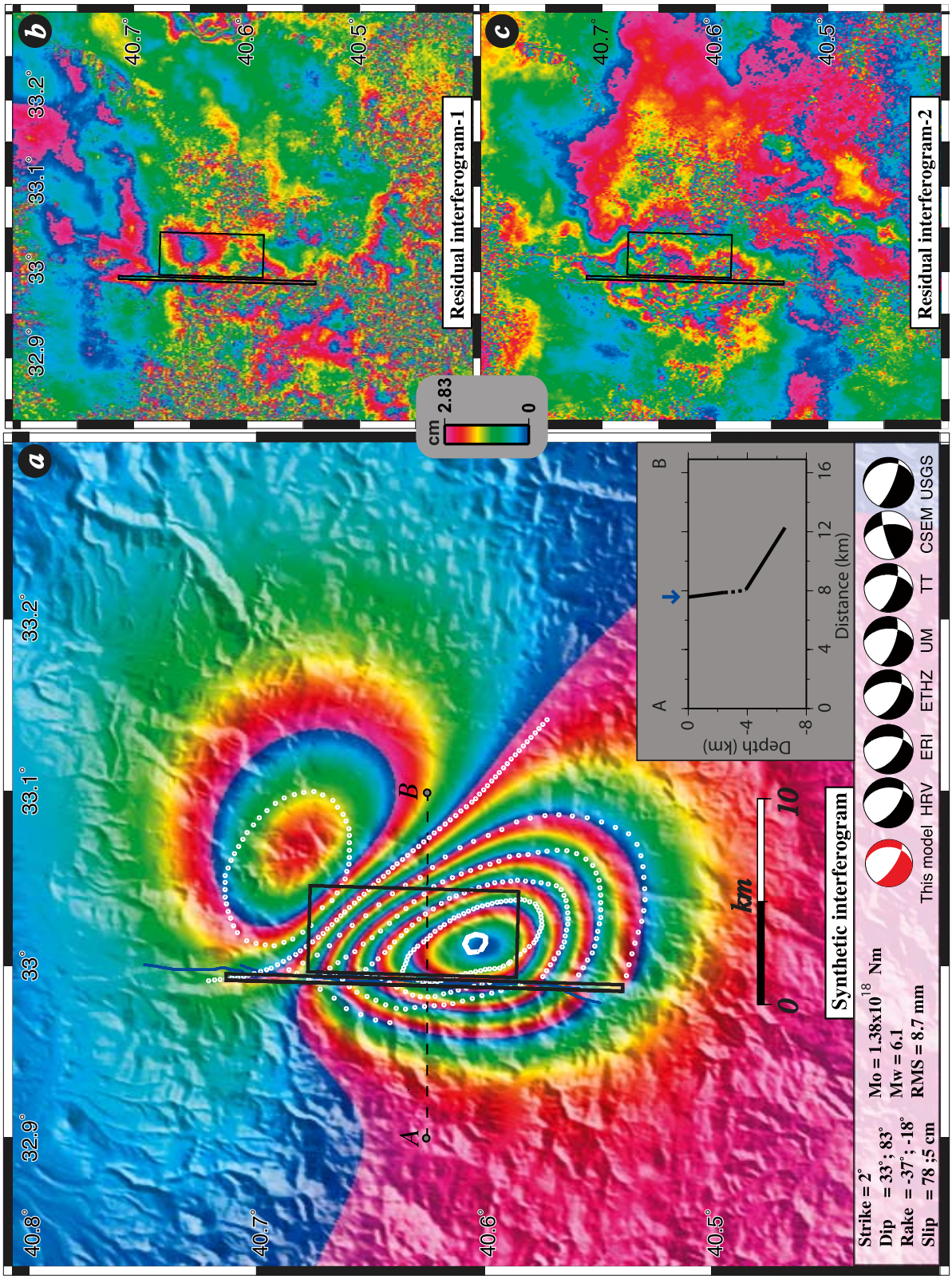
a
b
c
Residual interferogram-1
Residual interferogram-2
cm
2.83
0
Synthetic interferogram
Strike = 2°
Dip = 33°; 83°
Rake = -37°; -18°
Slip = 78 ;5 cm
Mo = 1.38x10^18 Nm
Mw = 6.1
RMS = 8.7 mm
This model HRV ERI ETHZ UM TT CSEM USGS
km
0
10
A
B
Depth (km)
Distance (km)
40.8°
40.7°
40.6°
40.5°
32.9°
33°
33.1°
33.2°

Figure 8

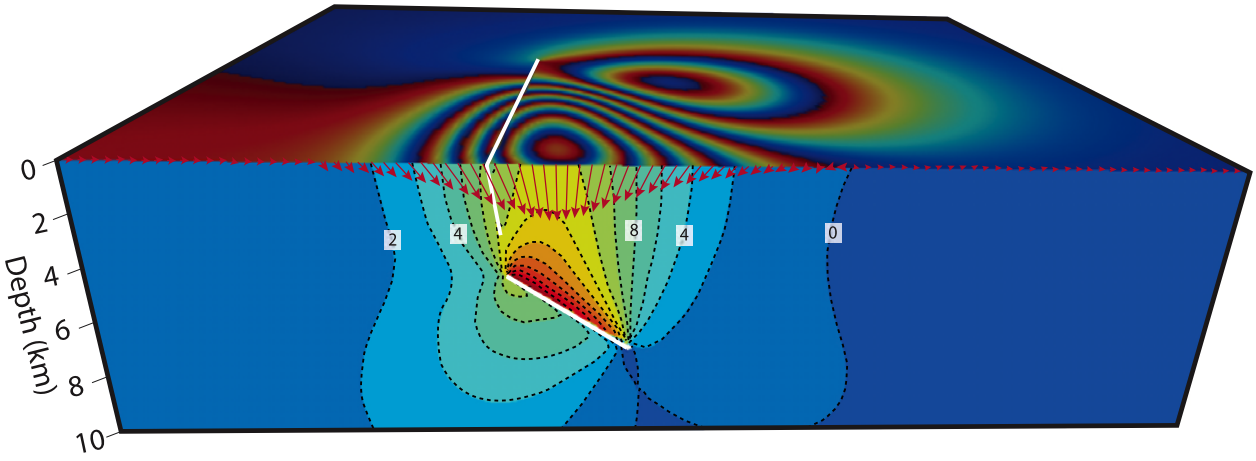

Figure 9. Three-dimensional perspective view of the interferogram predicted by the two-fault model, and the distribution of vertical displacements (with dashed contour lines in centimeters) on a fault-normal vertical section, constructed using the Poly3D boundary element program [*Thomas*, 1993; *Maerten et al.*, 2005]. Arrows indicate the direction and the magnitude of the surface displacement resolved on a fault-normal vertical plane.

triggered slip or possibly by the aftershock of magnitude 4 that occurred about 20 min later. Our Coulomb stress calculations show that slip on the low-angle fault promotes failure on the steep shallow fault by increasing the static stress on it by more than 10 bars. Thus, the minor shallow slip may have been triggered by the main shock in a similar way to the aseismic slip on the Shahdad thrust fault system triggered by the nearby 1998 oblique slip Fandoqa earthquake (M_w = 6.6) [*Fielding et al.*, 2004].

[21] We have calculated the orientation of the T axes from all the models with a fault dip ranging between 30° and 70° shown in Figure 5. Regardless of the change in fault dip or strike, the models show that the range of T axis orientation projected horizontally to the surface is fairly narrow and in the azimuth of N40 ± 7°E (Figure 6). This is consistent with those of focal mechanisms of earthquakes on the NAF in this region [*Taymaz et al.*, 2007], and with the orientations of the NAF and other faults, suggesting that the Dodurga fault is reactivated under the same present-day stress regime that governs the central western section of the NAF (Figure 6). Thus, the Dodurga fault may be considered as part of a broader plate-boundary deformation zone due to the restraining bend on this section of the NAF, instead of an evidence for internal deformation of the Anatolian block [e.g., *Utkucu et al.*, 2003; *Taymaz et al.*, 2007] where transpressional deformation causes the development of active thrust faults between NAF and Cerkes-Kursunlu valley (Figure 2) [see *Hubert-Ferrari et al.*, 2002, Figure 5].

[22] Faulting depth is well constrained and centered at ~5 km depth, in good agreement with inference of *Utkucu et al.* [2003] and *Taymaz et al.* [2007]. Although faulting took place at such a shallow depth, it did not quite reach to the surface, similarly to the 1994–2004 El Hoceima and 2003 Bam earthquakes [*Akoglu et al.*, 2006; *Fialko et al.*, 2005]. As estimated by *Utkucu et al.* [2003], the coseismic slip is perhaps too small (~40 cm) to reach to the surface. Otherwise, if it is as large as 2.3 m as inferred from waveform inversion by *Taymaz et al.* [2007], the shallow slip deficit can be attributed to the slip history of the fault. For example, accumulated strain on the uppermost 2–3 km part of the fault may have been released during the previous event. Therefore, it is impor-

Figure 8. (a) Synthetic interferogram predicted by the two-fault model, one dipping 83° at shallow depths (0–2.5 km) and the other dipping 33° at deeper depths (4.0–6.6 km). Inset box illustrates the relationship between the two faults in an east-west trending vertical cross section with a blue arrow showing the location of the Dodurga fault trace at surface. The two faults can be considered as a simple representation of a listric fault. See Figure 7 for the explanations of other symbols shown. (b and c) Residual interferograms as in Figure 7.

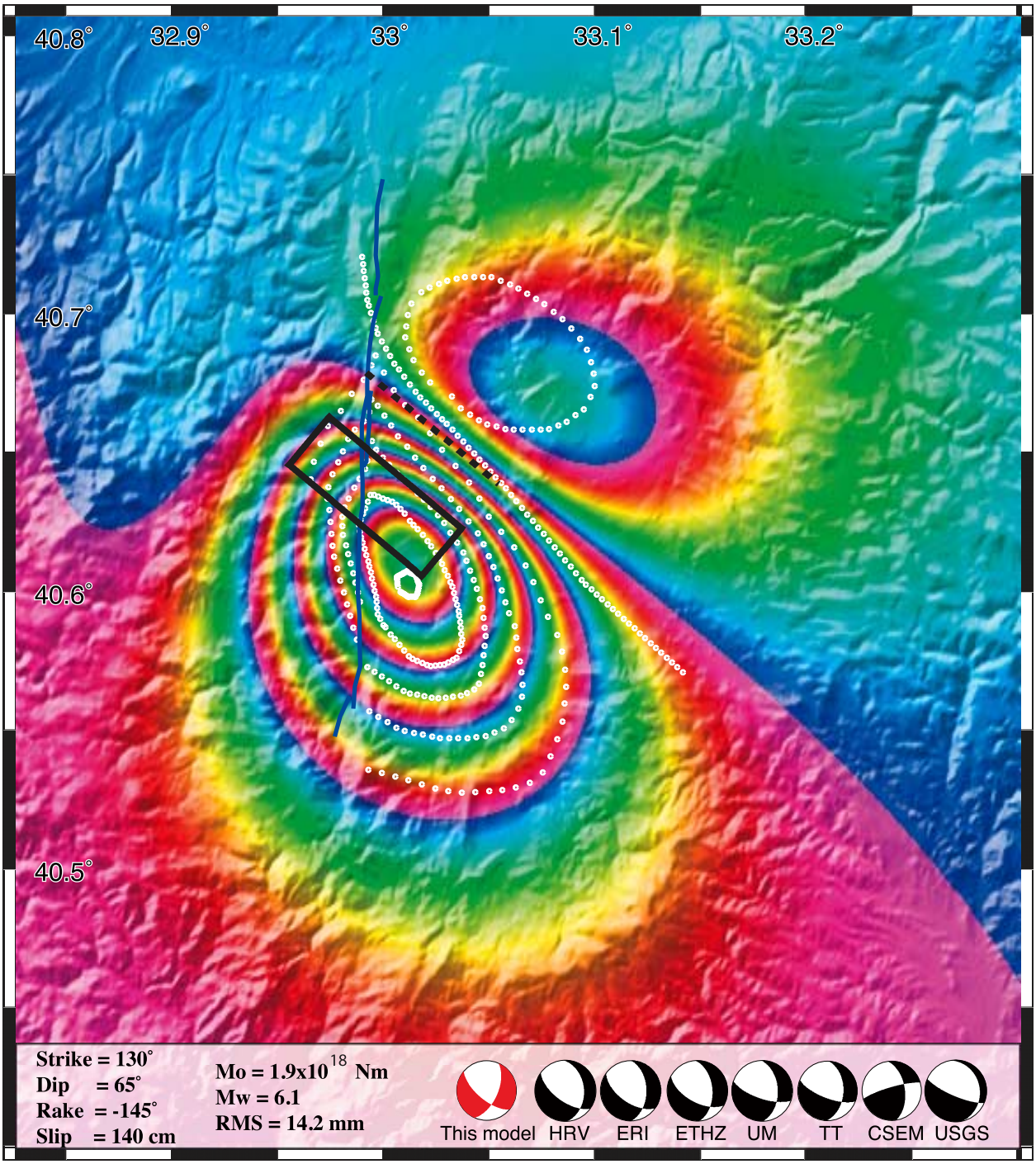

Figure 10. Model with ~140 cm of slip on a ~7 km long and ~5 km wide right-lateral fault trending NW–SE and dipping 65 SW° (at 5 to 10 km of depth). Although the misfit of the right-lateral solution is about ~40% higher than that of the best fitting two-fault model with left-lateral slip, it explains the overall fringe pattern of the coseismic interferograms.

tant to document distribution of coseismic slip on earthquake fault ruptures in order to understand the behavior and mechanism of active faults.

Acknowledgments

[23] InSAR data are copyrighted and obtained courtesy of the European Space Agency under the project AOTR-2436. We thank Gregory Lyzenga for providing the inversion code of Simplex program used in this study. We are grateful to Ömer Emre and Ali Pinar for their comments and criticisms in the ATAG11 meeting and Semih Ergintav and Mustapha Meghraoui for their suggestions. Critical reviews from Roland Bürgmann and Eric Fielding greatly improved the paper. We also thank Peter van Keken, the editor of the journal. A.M.A. is supported by EU-FP6 TR-Access Mobility Project, and Z.C. is supported by TUBITAK projects 107Y281 and 105G019. Most of the figures were plotted using GMT [*Wessel and Smith*, 1998].

References

Akoglu, A. M., Z. Cakir, M. Meghraoui, S. Belabbes, S. O. El Alami, S. Ergintav, and H. S. Akyuz (2006), The 1994–2004 Al Hoceima (Morocco) earthquake sequence: Conjugate fault ruptures deduced from InSAR, *Earth Planet. Sci. Lett.*, *252*(3–4), 467–480, doi:10.1016/j.epsl.2006.10.010.

Amelung, F., and J. W. Bell (2003), Interferometric synthetic aperture radar observations of the 1994 Double Spring Flat, Nevada, earthquake (*M5.9*): Main shock accompanied by triggered slip on a conjugate fault, *J. Geophys. Res.*, *108*(B9), 2433, doi:10.1029/2002JB001953.

Armijo, R., B. Meyer, A. Hubert, and A. Barka (1999), Westward propagation of the North Anatolian fault into the northern Aegean: Timing and kinematics, *Geology*, *27*(3), 267–270, doi:10.1130/0091-7613(1999)027<0267:WPOTNA>2.3.CO;2.

Armijo, R., B. Meyer, S. Navarro, G. King, and A. Barka (2002), Asymmetric slip partitioning in the Sea of Marmara pull-apart: A clue to propagation processes of the North Anatolian Fault?, *Terra Nova*, *14*(2), 80–86, doi:10.1046/j.1365-3121.2002.00397.x.

Barka, A. (1996), Slip distribution along the North Anatolian fault associated with the large earthquakes of the period 1939 to 1967, *Bull. Seismol. Soc. Am.*, *86*(5), 1238–1254.

Bernard, P., et al. (1997), The M_s=6.2, June 15, 1995 Aigion earthquake (Greece): Evidence for low normal faulting in the Corinth rift, *J. Seismol.*, *1*(2), 131–150.

Bozkurt, E. (2001), Neotectonics of Turkey: A synthesis, *Geodin. Acta*, *14*(1–3), 3–30, doi:10.1016/S09853111 (01)01066-X.

Bürgmann, R., P. A. Rosen, and E. J. Fielding (2000), Synthetic aperture radar interferometry to measure Earth's surface topography and its deformation, *Annu. Rev. Earth Planet. Sci.*, *28*, 169–209, doi:10.1146/annurev.earth.28.1.169.

Bürgmann, R., M. E. Ayhan, E. J. Fielding, T. J. Wright, S. McClusky, B. Aktug, C. Demir, O. Lenk, and A. Turkezer (2002), Deformation during the 12 November 1999 Duzce, Turkey, earthquake, from GPS and InSAR data, *Bull. Seismol. Soc. Am.*, *92*(1), 161–171, doi:10.1785/0120000834.

Cakir, Z., A. A. Barka, J. B. de Chabalier, R. Armijo, and B. Meyer (2003a), Kinematics of the November 12, 1999 (Mw = 7.2) Düzce earthquake deduced from SAR interferometry, *Turk. J. Earth Sci.*, *12*(1), 105–118.

Cakir, Z., J. B. de Chabalier, R. Armijo, B. Meyer, A. Barka, and G. Peltzer (2003b), Coseismic and early post-seismic slip associated with the 1999 Izmit earthquake (Turkey), from SAR interferometry and tectonic field observations, *Geophys. J. Int.*, *155*(1), 93–110, doi:10.1046/j.1365-246X.2003.02001.x.

Cakir, Z., A. M. Akoglu, S. Belabbes, S. Ergintav, and M. Meghraoui (2005), Creeping along the Ismetpasa section of the North Anatolian fault (western Turkey): Rate and extent from InSAR, *Earth Planet. Sci. Lett.*, *238*(1–2), 225–234, doi:10.1016/j.epsl.2005.06.044.

Cakir, Z., M. Meghraoui, A. M. Akoglu, N. Jabour, S. Belabbes, and L. Ait-Brahim (2006), Surface deformation associated with the M_w 6.4, 24 February 2004 Al Hoceima, Morocco, earthquake deduced from InSAR: Implications for the active tectonics along North Africa, *Bull. Seismol. Soc. Am.*, *96*(1), 59–68, doi:10.1785/0120050108.

Donnellan, A., and G. A. Lyzenga (1998), GPS observations of fault afterslip and upper crustal deformation following the Northridge earthquake, *J. Geophys. Res.*, *103*(B9), 21,285–21,297, doi:10.1029/98JB01487.

Emre, Ö., T. Y. Duman, A. Doğan, and S. Özalp (2000), Evaluation Report of the 6 June 2000 Orta (Çankiri-Turkey) earthquake (in Turkish), Geol. Dep., MTA, Ankara.

Farr, T. G., et al. (2007), The Shuttle Radar Topography Mission, *Rev. Geophys.*, *45*, RG2004, doi:10.1029/2005RG000183.

Fialko, Y., D. Sandwell, M. Simons, and P. Rosen (2005), Three-dimensional deformation caused by the Bam, Iran, earthquake and the origin of shallow slip deficit, *Nature*, *435*, 295–299, doi:10.1038/nature03425.

Fielding, E. J., T. J. Wright, J. Muller, B. E. Parsons, and R. Walker (2004), Aseismic deformation of a fold-and-thrust belt imaged by synthetic aperture radar interferometry near Shahdad, southeast Iran, *Geology*, *32*(7), 577–580, doi:10.1130/G20452.1.

Flerit, F., R. Armijo, G. C. P. King, B. Meyer, and A. Barka (2003), Slip partitioning in the Sea of Marmara pull-apart determined from GPS velocity vectors, *Geophys. J. Int.*, *154*(1), 1–7, doi:10.1046/j.1365-246X.2003.01899.x.

Freed, A. M., R. Bürgmann, E. Calais, J. Freymueller, and S. Hreinsdóttir (2006), Implications of deformation following the 2002 Denali, Alaska, earthquake for postseismic relaxation processes and lithospheric rheology, *J. Geophys. Res.*, *111*, B01401, doi:10.1029/2005JB003894.

Gabriel, A. K., R. M. Goldstein, and H. A. Zebker (1989), Mapping small elevation changes over large areas: Differential radar interferometry, *J. Geophys. Res.*, *94*(B7), 9183–9191, doi:10.1029/JB094iB07p09183.

Goldstein, R. M., and C. L. Werner (1998), Radar interferogram filtering for geophysical applications, *Geophys. Res. Lett.*, *25*(21), 4035–4038, doi:10.1029/1998GL900033.

Hanssen, R. F. (2001), *Radar Interferometry: Data Interpretation and Error Analysis*, Kluwer Acad., Dordrecht, Netherlands.

Hubert-Ferrari, A., R. Armijo, G. King, B. Meyer, and A. Barka (2002), Morphology, displacement, and slip rates along the North Anatolian Fault, Turkey, *J. Geophys. Res.*, *107*(B10), 2235, doi:10.1029/2001JB000393.

Jackson, J. A., J. Gagnepain, G. Houseman, G. C. P. King, P. Papadimitriou, C. Soufleris, and J. Virieux (1982), Seismicity, normal faulting, and the geomorphological development of the Gulf of Corinth (Greece)—The Corinth earthquakes of February and March 1981, *Earth Planet. Sci. Lett.*, *57*(2), 377–397, doi:10.1016/0012-821X(82)90158-3.

Jònsson, S., H. Zebker, P. Segall, and F. Amelung (2002), Fault slip distribution of the 1999 Hector Mine, California, earthquake, estimated from satellite radar and GPS measurements, *Bull. Seismol. Soc. Am.*, *92*(4), 1377–1389, doi:10.1785/0120000922.

Kocyigit, A., B. Rojay, B. Cühan, and A. Özacar (2001), The June 6, 2000, Orta (Cankiri, Turkey) earthquake: Sourced from a new antithetic sinistral strike-slip structure of the North Anatolian Fault system, the Dodurga Fault Zone, *Turk. J. Earth Sci.*, *10*, 69–82.

Kozaci, O., J. Dolan, R. Finkel, and R. Hartleb (2007), Late Holocene slip rate for the North Anatolian fault, Turkey, from cosmogenic Cl-36 geochronology: Implications for the constancy of fault loading and strain release rates, *Geology*, *35*, 867–870, doi:10.1130/G23187A.1.

Maerten, F., P. Resor, D. Pollard, and L. Maerten (2005), Inverting for slip on three-dimensional fault surfaces using angular dislocations, *Bull. Seismol. Soc. Am.*, *95*(5), 1654–1665, doi:10.1785/0120030181.

Massonnet, D., and K. L. Feigl (1998), Radar interferometry and its application to changes in the Earth's surface, *Rev. Geophys.*, *36*(4), 441–500, doi:10.1029/97RG03139.

Massonnet, D., M. Rossi, C. Carmona, F. Adagna, G. Peltzer, K. Feigl, and T. Rabaute (1993), The displacement field of the Landers earthquake mapped by radar interferometry, *Nature*, *364*(8), 138–142, doi:10.1038/364138a0.

McClusky, S., et al. (2000), Global Positioning System constraints on plate kinematics and dynamics in the eastern Mediterranean and Caucasus, *J. Geophys. Res.*, *105*(B3), 5695–5719.

McClusky, S., R. Reilinger, S. Mahmoud, D. Ben Sari, and A. Tealeb (2003), GPS constraints on Africa (Nubia) and Arabia plate motions, *Geophys. J. Int.*, *155*(1), 126–138, doi:10.1046/j.1365-246X.2003.02023.x.

Okada, Y. (1985), Surface deformation due to shear and tensile faults in a half-space, *Bull. Seismol. Soc. Am.*, *75*(4), 1135–1154.

Reilinger, R., et al. (2006), GPS constraints on continental deformation in the Africa-Arabia-Eurasia continental collision zone and implications for the dynamics of plate interactions, *J. Geophys. Res.*, *111*, B05411, doi:10.1029/2005JB004051.

Rosen, P. A., S. Hensley, G. Peltzer, and M. Simons (2004), Updated Repeat Orbit Interferometry package released, *Eos Trans. AGU*, *85*(5), 47, doi:10.1029/2004EO050004.

Saroglu, F., Ö. Emre, and I. Kuşçu (1992), *Active Fault Map of Turkey*, Gen. Dir. of Miner. Res. and Explor., Ankara.

Scharroo, R., and P. Visser (1998), Precise orbit determination and gravity field improvement for the ERS satellites, *J. Geophys. Res.*, *103*(C4), 8113–8127, doi:10.1029/97JC03179.

Sengör, A. M. C., N. Görür, and F. Saroglu (1985), Strike-slip faulting and related basin formation in zones of tectonic escape: Turkey as a case study, in *Strike-Slip Deformation, Basin Formation, and Sedimentation*, edited by K. T. Biddle and N. Christie-Blick, *Spec. Publ. Soc. Econ. Paleontol. Mineral.*, *37*, 227–264.

Sengör, A. M. C., O. Tüysüz, C. İmren, M. Sak̃nç, H. Eyidoğan, N. Gorur, X. Le Pichon, and C. Rangin (2005), The North Anatolian Fault: A new look, *Annu. Rev. Earth Planet. Sci.*, *33*(1), 37–112, doi:10.1146/annurev.earth.32.101802.120415.

Talebian, M., et al. (2004), The 2003 Bam (Iran) earthquake: Rupture of a blind strike-slip fault, *Geophys. Res. Lett.*, *31*, L11611, doi:10.1029/2004GL020058.

Taymaz, T., T. J. Wright, S. Yolsal, O. Tan, E. Fielding, and G. Seyitoğlu (2007), Source characteristics of the 6 June 2000 Orta Çank̃r (central Turkey) earthquake: A synthesis of seismological, geological and geodetic (InSAR) observations, and internal deformation of the Anatolian plate, in *The Geodynamics of the Aegean and Anatolia*, edited by T. Taymaz et al., *Geol. Soc. Spec. Publ.*, *291*, 259–290.

Thomas, A. L. (1993), Poly3D: A three-dimensional, polygonal element, displacement discontinuity boundary element computer program with applications to fractures, faults, and cavities in the Earth's crust, M.Sc. thesis, 221 pp., Stanford Univ., Stanford, Calif.

Toksöz, M. N., A. F. Shakal, and A. J. Michael (1979), Space-time migration of earthquakes along the North-Anatolian fault zone and seismic gaps, *Pure Appl. Geophys.*, *117*(6), 1258–1270, doi:10.1007/BF00876218.

Utkucu, M., O. Alptekin, and A. Pinar (2003), A detailed source study of the Orta (Cankiri) earthquake of June 6, 2000 (M_s = 6.1), an intraplate earthquake in central Anatolia, *J. Seismol.*, *7*(2), 193–202, doi:10.1023/A:1023566626611.

Wells, D. L., and K. J. Coppersmith (1994), New empirical relationships among magnitude, rupture length, rupture width, rupture area, and surface displacement, *Bull. Seismol. Soc. Am.*, *84*(4), 974–1002.

Wessel, P., and W. H. F. Smith (1998), New, improved version of Generic Mapping Tools released, *Eos Trans. AGU*, *79*(47), 579, doi:10.1029/98EO00426.

Westaway, R. (1999), The mechanical feasibility of low-angle normal faulting, *Tectonophysics*, *308*(4), 407–443, doi:10.1016/S0040-1951(99)00148-1.

Wright, T., E. Fielding, and B. Parsons (2001a), Triggered slip: Observations of the 17 August 1999 Izmit (Turkey) earthquake using radar interferometry, *Geophys. Res. Lett.*, *28*(6), 1079–1082, doi:10.1029/2000GL011776.

Wright, T., B. Parsons, and E. Fielding (2001b), Measurement of interseismic strain accumulation across the North Anatolian Fault by satellite radar interferometry, *Geophys. Res. Lett.*, *28*(10), 2117–2120, doi:10.1029/2000GL012850.

Zebker, H. A., P. A. Rosen, R. M. Goldstein, A. Gabriel, and C. L. Werner (1994), On the derivation of coseismic displacement fields using differential radar interferometry: The Landers earthquake, *J. Geophys. Res.*, *99*(B10), 19,617–19,634, doi:10.1029/94JB01179.

Zebker, H. A., P. A. Rosen, and S. Hensley (1997), Atmospheric effects in interferometric synthetic aperture radar surface deformation and topographic maps, *J. Geophys. Res.*, *102*(B4), 7547–7563, doi:10.1029/96JB03804.